Load-Adaptive Resonant Frequency-Tuned Δ-Σ Pulse Density Modulation for Class-D ZVS High-Frequency Inverter-Based Inductive Wireless Power Transfer

Mishima, Tomokazu

Lai, Ching-Ming

Load-Adaptive Resonant Frequency-Tuned Δ-Σ Pulse Density Modulation for Class-D ZVS High-Frequency Inverter-based Inductive Wireless Power Transfer

Tomokazu Mishima, *Senior Member*, and Ching-Ming Lai, *Senior Member*

***Abstract*—This paper presents a resonant frequency tuning (RFT) Delta-Sigma (Δ-Σ) signal-transformed pulse density modulation (PDM) class-D converter for inductive power transfer (IPT) applications. The proposed power controller provides a load-adaptive pulse modulation by tuning a zero phase angle (ZPA) and peak-power frequency, i.e. resonant frequency in the primary-side high frequency inverter. The switching frequency is regulated in accordance with the variations of the load and coupling co-efficient between the transmitting (Tx) and receiving (Rx) coils. The output power is controlled by the RFT-$\Delta\Sigma$ PDM which is effective for reducing a low frequency oscillation (subharmonics), thereby the high efficiency power transmission can attain. The essential performances of the proposed IPT power controller are demonstrated in experiment of a $400\mathrm{W}$-$500\mathrm{kHz}$ of prototype, whereby the feasibility is clarified from a practical point of view.**

***Index Terms*—Class-D power converter, delta-sigma (Δ-Σ) signal transformation, inductive power transfer (IPT), pulse density modulation (PDM), resonant frequency tuning (RFT), series resonant, soft switching.**

I. Introduction

A Critical technical concern for the modern IPT systems is how to carry out power regulation with an effective pulse modulation strategy of switching pulse patterns. Fig. 1 illustrates their typical power process and control schemes. The power control strategies suitable for the resonant power converter in IPTs are categorized as; pulse amplitude modulation (PAM) [1] [2], pulse width modulation (PWM) [3]-[6], single or dual phase shift (SPS, DPS) modulation [7] [8], pulse-frequency-modulation (PFM) [9] [10], and pulse density modulation (PDM) [13]- [20]. The existing power control strategies are briefly summarized in TABLE I.

The dual-side controls with DPS are the research-oriented topics; the front-end dc chopper-based PAM in transmitter (Tx) coils [21], the rear-end dc chopper-based PWM in receiver (Rx) coils, and the active rectifier-based PWM in Rx coils. This concept of power control is based on the impedance regulation in accordance with the load conditions. However, the structures of power circuit and controller are inevitably complicated in order to detect both the Tx and Rx coil currents and process the multi modulations of duty cycles with significant amount of circulating current paying for soft switching. As a counterpart, the single-side power control is primitive, but practical and still attractive for IPT applications with the advance of compensation topologies, Tx-Rx coils, signal communication processing, sensors and the switching power devices. In addition, the Tx-side power control scheme is the effective solution in the case on the emerging applications such as biomedical implantable wireless power transfer (WPT). Accordingly, it is worthwhile revisit the primary-side power controller and propose the new solution in this paper.

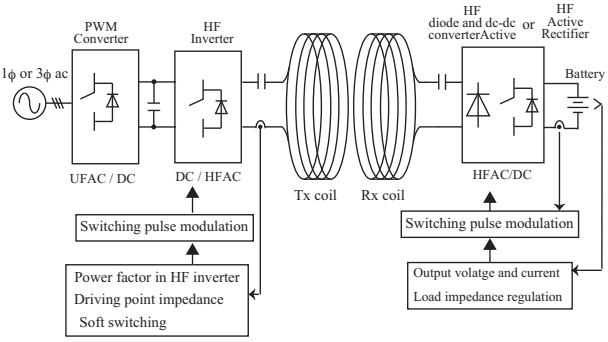

Fig. 1. Power conversion and control system for IPT system.

The typical Tx side-based IPT power control schemes are divided into PFM, asymmetrical PWM (A-PWM), phase shifty PWM (PS-PWM), and PDM. PFM function of load resonant frequency tuning, i.e. natural oscillation frequency tuning, but is involved with a wide range of switching frequency variations; thus, it is not suitable for IPT systems under the severer condition of electromagnetic interference [22]. A-PWM and PS-PWM suffer from severe hard switching, and circulating current respectively, as a result system efficiency will deteriorate in the light load conditions. The PWM and PFM hybrid scheme is discussed and evaluated in [23] with

T. Mishima, the corresponding author is with the Div. of Marine Technologies and Engineering, Faculty of Oceanology, and Center for Advanced Medical Engineering Research and Development (CAMED), Kobe University, Hyogo, Japan (e-mail: mishima@maritime.kobe-u.ac.jp.

C.M. Lai is with the Department of Electrical Engineering, National Chung Hsing University, Taichung, Taiwan (e-mail: pecmlai@nchu.edu.tw).

This article has been accepted for publication in a future issue of this journal, but has not been fully edited. Content may change prior to final publication. Citation information: DOI 10.1109/JESTIE.2021.3102445, IEEE Journal of Emerging and Selected Topics in Industrial Electronics

the maximum power point tracking base on the dc input power. This scheme may suffer from the double-frequency power pulsation at the dc-link stage in a single-phase system.

In contrast to those technical problems, the Tx side-based PDM ensures a wider range of soft switching, less count of component, and constant or limited switching frequency, and last but not least availability of natural oscillation. The methodologies of PDM signal patters are divided into a burst mode [17] [18], lookup-table sequence [13], [19], and Δ-Σ transformation [14], [20]. Fig. 2 illustrates the three PDM patterns together with Tx-coil currents in a half-bridge (Class-D) HF inverter. The burst-mode PDM suffers from subharmonics and parasitic ringings in the Tx and Rx-coil currents and hard switching appears in the light load condition. The lookup-table sequence PDM can reduce the subharmonics and parasitic ringings to some extent, however the low-resolution of power control due to the limited pattern of switching sequence are still obstacle for the practical IPT systems as well as the burst-mode PDM. The Δ-Σ modulator converts the analog value to the random pulse pattern, accordingly the low frequency subharmonics are eliminated effectively in the output power, As a result, voltage ripple reduction of the output filter and excellent soft switching performances independent of load powers can be expected [24]. In addition, noise shaping, i.e. mitigation of low frequency noises and moving them to higher band are attractive features of Δ-Σ modulator, which works effectively for reduction of electro magnetic interference in IPT systems. The excellent dynamic response for variation of command signals (load voltage/current) can be expected in Δ-Σ modulator, which is beneficial for the Tx side-based power control in IPT systems considering the propagation delay between Tx and Rx sides. However, the existing Δ-Σ PDM solutions have not been considered for the load resonant frequency variations due to the change of coupling co-efficient. Accordingly, performances of zero-voltage soft switching (ZVS) significantly depends on the loaded quality factor. In addition, there is no clear discussion on how to adjust and manage the PDM ratio by taking the load condition into account. The preceding paper [19] proposes a natural oscillation-based Δ-Σ PDM, however a method of resonant frequency tuning (RFT) and its verification are not discussed in details.

The RFT methodologies in the past literatures [10] [11], [25]- [27] deals with the driving point impedance and zero phase angle (ZPA) just for obtaining maximum power and achieving ZVS. The reference [11] utilizes frequency tuning for air and underwater WPT applications, whereby the pre-design method is adopted for resonant frequency of series-series resonant tanks (SS) and dynamical tuning is not discussed in details. The voltage and frequency tuning method is prosed in [12], however the phase angle for assuring ZVS in the active switches are not considered in the analysis, design and verification. The PDM-based hybrid IPT topologies have been proposed by featuring ZPA and robustness to the misalignment of Tx and Rx coils [28]. However, the multiple combination of resonant tanks and coils may not be suitable for downsizing IPT systems such as the human body implantable wireless power transfer (WPT) [29]. The parallel capacitor-based ZPA tuning method is proposed in [30], however is limited to current-source IPT circuit topology.

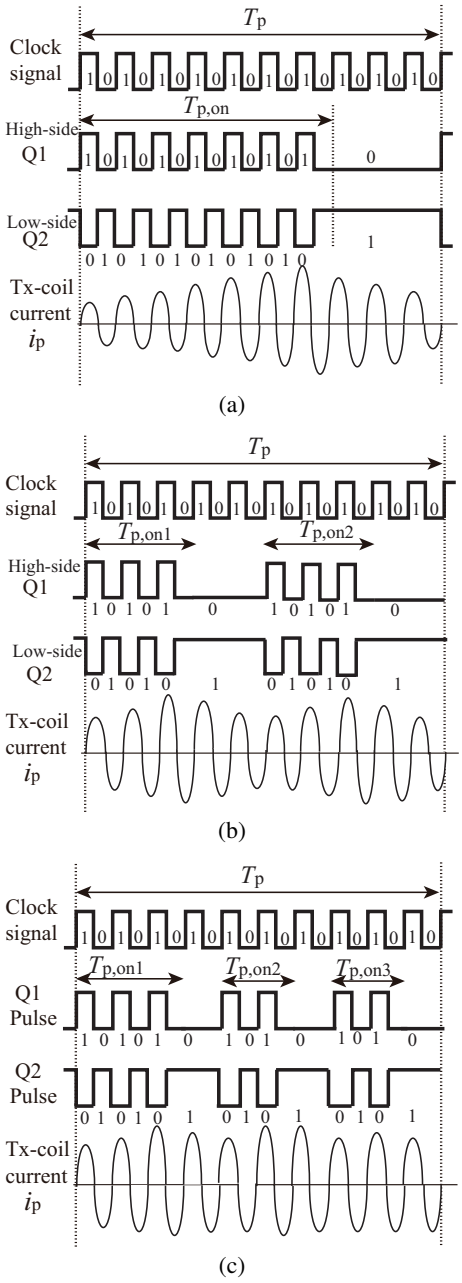

Fig. 2. PDM patters and Tx-coil current: (a) burst mode, (b) pre-defined sequence, and (c) Δ-Σ transformation.

As a solution for the technical issues of those existing strategies, RFT and Δ-Σ PDM-based Tx-side power control is originally proposed in this paper. The challenging aspect of the power controller is how to control the output power without any extra dc-dc converter nor active rectifier in the receiver side while keeping ZVS in the class-D high frequency inverter without depending on the loaded quality factor of the main circuit. The main and unique technologies are; RFT contributes for determining the load resonant and ZPA frequencies and optimizing the driving point impedance in accordance with the variations of coupling co-efficient and load; Δ-Σ PDM

TABLE I
COMPARISON OF ESSENTIAL PERFORMANCES AND CHARACTERISTICS OF IPT POWER CONTROL METHODS

Modulation references♯	Topology resonant tank	Power rating / Switching frequency	Power factor for ZPA	Soft switching
PAM [1] [2]	rear-end buck chopper	40 W / 13.56 MHz	uncontrolled	N / A
PWM [3]- [16]	full-bridge inverter active rectifiers	$1-3$ kW / 85 kHz	uncontrolled	ZVS
SPS, DPS [7] [8]	dual active bridge	3 kW/35 kHz	NOT specified	ZVS
PFM [9]– [12], [26]	half or full bridge inverter	1 kW / 70 kHz	controlled	ZCS
PDM [13] [15] [19] [20]	half or full bridge inverter	0.1-1 kW / 85 kHz-6.78 MHz	NOT specified	ZVS

operates for controlling the load power with keeping small transitional interval and maintaining ZVS. The fast response of Δ-Σ signal transformation helps to compensate the dynamics of Tx side-based power controller to the load variations although it is not competitive as the secondary side (Rx side)-based control scheme. Furthermore, correlation among resonant frequencies of the multi-resonant tanks, natural oscillation frequency, i.e. load resonant frequency and ZPA is originally demonstrated by using the Extra Element Theorem of R.D. Middlebrook [31]; this analytical approach paves the way for a practical design methodology of any types of resonant tanks in IPT systems.

The rest of paper is organized as follows; the circuit topology and principle of power factor correction in a high frequency inverter are explained in Section. II. The controller scheme of the proposed RFT-$\Delta\Sigma$PDM is explained and the similarity between a resonant frequency and the natural frequency of the main circuit is demonstrated in Section III, whereby the principle of the proposed pulse modulation strategy is clarified in terms of high power factor and soft switching range. The practical effectiveness of the proposed power controller is verified by experiment of a 400 W-500 kHz prototype in Section IV. The essential features of the proposed IPT system are summarized in Section V.

II. CIRCUIT TOPOLOGY AND OPERATION PRINCIPLE

A. Main Circuit

The circuit diagram of the Class-D ZVS resonant converter with the proposed RFT-$\Delta\Sigma$PDM is illustrated in Fig. 3. ZVS turn-on and the nearly zero current soft switching (ZCS) turn-off can achieve in the active switches Q_1 and Q_2 by utilizing their output capacitances and the leakage inductance of the Tx coil. The resonant frequencies f_{r1}, f_{r2} of the primary and secondary compensators in SS topology are defined as

$$f_{r1} = \frac{1}{2\pi\sqrt{L_1 C_1}}, \quad f_{r2} = \frac{1}{2\pi\sqrt{L_2 C_2}} \tag{1}$$

, which are tuned identically as $f_r = f_{r1} = f_{r2}$.

ZVS commutation can sustain between the power-OFF and power-ON intervals due to synchronization of the switching frequency with the natural oscillation frequency. It is achievable in the case of loosely coupling that is characterized with a unimodal ZPA point since the two frequencies are

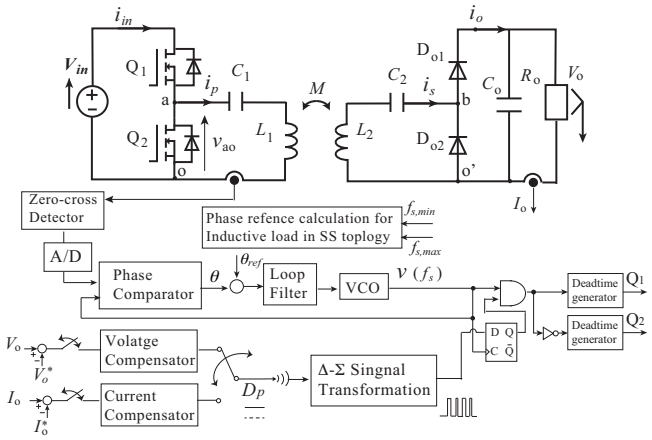

Fig. 3. Proposed RFT-$\Delta\Sigma$PDM ZVS resonant converter for IPT.

almost identical. However, it is necessary to search for the natural oscillation frequency and track it under the condition of a slightly loose coupling or relatively tight coupling that contains multiple ZPA points, i.e. the frequency spurious. The novelty of the proposed control scheme is to tuning the resonant frequency that corresponds to a natural oscillation frequency and ZPA point while activating the Δ-Σ PDM for load power regulation. Combination of Δ-Σ PDM and class-D inverter makes only the low side switch keep ON-state for controlling output power, and eliminate the additional resonant tank branch for sustaining the oscillation whereas it is indispensable for a full-bridge inverter-based PDM IPT [32].

B. Controller Scheme

The power controller consists of mainly two parts; the lagging-phase PLL-based frequency tuning for ZVS, and the output voltage and current compensator loop for deterring the duty cycle of PDM. Although the dual control loops of voltage and current are fundamental for constant current and constant voltage (CCCV) mode of a battery charging, the voltage control is mainly treated herein for simplifying of discussion on the performance of the Δ-Σ PDM.

The Tx coil current i_p is detected and transformed to the pulse signal via the zero-cross-detector, after which the phase difference is calculated with respect to the output pulse signal

This article has been accepted for publication in a future issue of this journal, but has not been fully edited. Content may change prior to final publication. Citation information: DOI 10.1109/JESTIE.2021.3102445, IEEE Journal of Emerging and Selected Topics in Industrial Electronics

v_f of the voltage-controlled-oscillator (VCO). It should be remarked herewith v_p corresponds to the bridge-leg voltage v_{ao} in the class-D high frequency inverter. The phase angle θ_o is compared with its reference θ_{ref}, then v_f is produced by proportional and integrator compensator-based VCO in the RFT controller loop while it works as the clock signal i.e. the switching frequency f_s in Δ-Σ PDM. The reference angle θ_{ref} is set so as to obtain the lagging-phase current in the HF inverter for achieving ZVS.

The PDM rate, i.e. pulse density D_p is determined in the voltage /current controller of the dc load with its command value V_o^* / C_o^*, then is transmitted through the wireless communicator to Δ-Σ modulator. The Δ-Σ modulator includes an integrator and a comparator, followed by a D flip-flop that synchronizes with the clock signal v_f. The Δ-Σ signal modulator reduces the low-frequency ripple in v_o due to the effect of random noise spectrums in the switching pulse pattern in contrast to "ON-OFF" control [33]. The variable frequency and variable duty-cycle pulse can be produced by combining with RFT. As a result, the random but weighted switching patterns can be generated so that the dc command signal D_p is compensated by the quantum signal Q in the D flip-flop circuit. The signal Q is synchronized with the output signal of VCO, accordingly the transitions between power-ON and -OFF periods are well shorten.

III. Analysis and Design Guideline

A. Equivalent Circuits and Analysis

The logic circuit diagram of the Δ-Σ modulator is depicted in Fig. 4(a). The pulse signal Q which is feedback from the inner D flip-flop is compared with the analog signal D_p (Δ function) which reflects on the load voltage control, and its output pulse signal weighted by D_p is integrated to produce the variable amplitude and slew rate sawtooth wave v_{sat} (Σ function) in random. Accordingly, the variable frequency and variable duty cycle pulse v_{comp} can be obtained.

In addition, the pulse patterns of the proposed controller are drawn in Fig. 4(b) on the basis of Δ-Σ transformation. The power-ON and -OFF periods of PDM are randomly dispersed under the principle of Δ-Σ signal transformation. Accordingly, the low-frequency subharmonics oscillation of i_p can be minimized.

The pulse density D_p is defined as

$$D_p = \frac{\sum_{k=1}^{n} T_{p,on,k}}{T_p}. \tag{2}$$

By applying the sinusoidal wave approximation and Fourier series analysis, the fundamental frequency component $v_{ao,1}$ of v_{ao} in the primary-side inverter is obtained U_s by the root mean square (RMS) value as

$$U_s = V_{ao,1} = \frac{\sqrt{2}D_p}{\pi} V_1. \tag{3}$$

The self inductances of Tx and Rx coils can be expressed by a HF transformer for facilitating a frequency-domain analysis of the power circuits [16], [34]. Fig. 5 shows the simplified equivalent circuit of the IPT ZVS converter with the equivalent

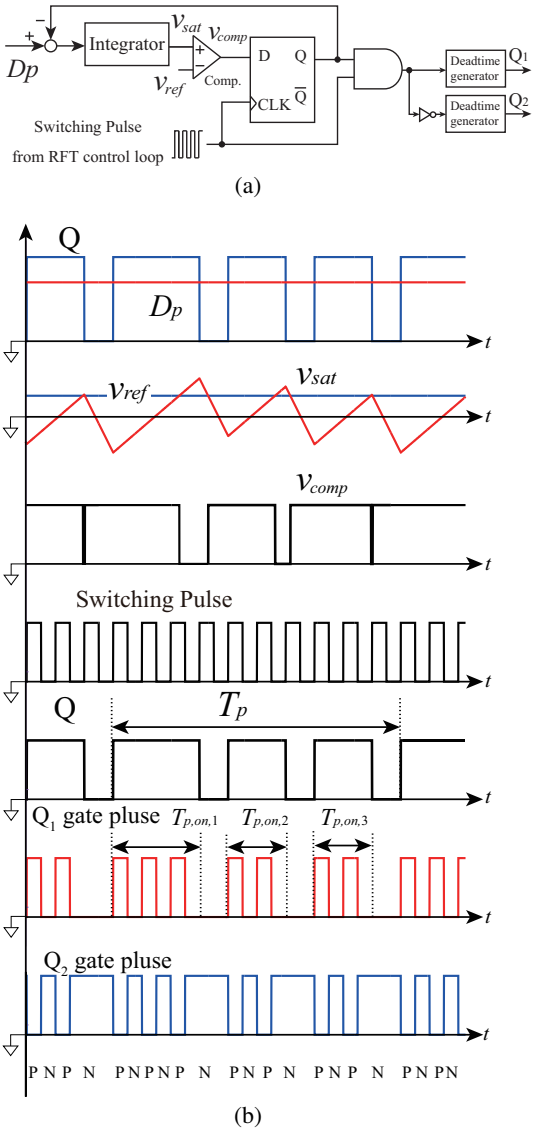

Fig. 4. Δ-Σ modulator and relevant waveforms: (a) logic circuit diagram, and (b) signals and pulses ($D_p = 0.7$) Q_1 ON/ Q_2 OFF; state-P, Q_1 OFF/ Q_1 OFF; state-O, and Q_1 OFF/ Q_2 ON; state-N.

ac resistance R_{ac} ($= 2a'^2 R_o/\pi^2$). Note in Fig. 5 the windings turns ratio of Tx and Rx coils a ($= \sqrt{L_1/L_2}$) is redefined as a' with the coupling co-efficient k so that the leakage inductance of the Rx coil is included in the Tx coil as expressed by

$$a' = \frac{M}{L_2} = k\sqrt{\frac{L_1}{L_2}}. \tag{4}$$

Accordingly, the leakage inductance L_r and magnetizing inductance L_m of Tx and Rx coils are denoted as $L_r = (1-k^2)L_1$ and $L_m = k^2 L_1$.

The transmitted power from the class-D HF inverter is expressed as

$$P_1 = \frac{|\dot{Z}_2|U_s^2}{|\dot{Z}_1\dot{Z}_2| + Z_m^2} \propto D_p^2 \tag{5}$$

where Z_1, Z_2 and Z_m are written from Fig. 5 with the angular switching frequency ω ($= 2\pi f_s$) as $\dot{Z}_1 = r_1 + j(\omega L_r -$

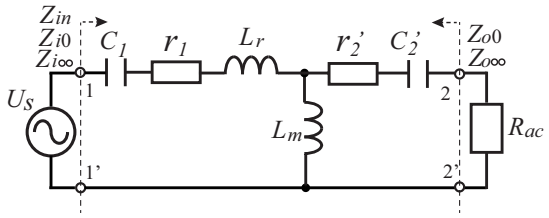

Fig. 5. Simplified equivalent circuit of a SS topology ($L_r = (1-k^2)L_1$, $L_m = k^2 L_1$, $r_2{}' = a'^2 r_2$, and ${C_2}^2 = C_2/a'^2$).

$1/\omega C_1\big)$, $\dot{Z}_2 = \big(r_2{}' + 1/j\omega C_2{}'\big)$ and $\dot{Z}_m = j\omega L_m$. Thus, it can be understood from (5) the transmitted power P_1 is proportion to square of D_p when the power factor of the HF inverter is ideally one.

The driving point impedance Z_{in} in Fig 5 can be revealed by adopting the Middlebrook's Extra Element Theorem as [31]

$$\dot{Z}_{in} = \dot{Z}_{i0}\frac{1+\frac{R_{ac}}{\dot{Z}_{o0}}}{1+\frac{R_{ac}}{\dot{Z}_{o\infty}}} = \dot{Z}_{i\infty}\frac{1+\frac{\dot{Z}_{i0}}{R_{ac}}}{1+\frac{\dot{Z}_{i\infty}}{R_{ac}}} \tag{6}$$

where the four impedances Z_{i0}, $Z_{i\infty}$, Z_{o0} and $Z_{o\infty}$ are written as

$$\dot{Z}_{i0} = r_1 + j\big(\omega L_r - \frac{1}{\omega C_1}\big) + j\omega L_m // \left(r_2{}' + \frac{1}{j\omega C_2{}'}\right) \tag{7}$$

$$\dot{Z}_{i\infty} = r_1 + j\omega\left(L_r + L_m\right) + \frac{1}{j\omega C_1} \tag{8}$$

$$\dot{Z}_{o0} = \left(r_2{}' + \frac{1}{j\omega C_2{}'}\right) + j\omega L_m // \left(r_1 + j\omega L_r + \frac{1}{j\omega C_1}\right) \tag{9}$$

$$\dot{Z}_{o\infty} = \left(r_2{}' + \frac{1}{j\omega C_2{}'}\right) + j\omega L_m. \tag{10}$$

Based on (6)–(10), the driving-point impedance of the class-D resonant inverter and rectifier with SS compensation is expressed by frequency-domain function Z_{in} in (11).

B. Frequency Tuning Around ZPA

The resonant frequency of the SS resonant tank including the Tx and Rx coils can be derived by solving $Z_{o0}(s) = 0$ in (9) as

$$f_{r1} = \sqrt{\frac{\Gamma^2 - \sqrt{\Gamma^2 - 4{f_{rs}}^2{f_{ms}}^2}}{2}} \tag{12}$$

$$f_{r2} = \sqrt{\frac{\Gamma^2 + \sqrt{\Gamma^2 - 4{f_{rs}}^2{f_{ms}}^2}}{2}} \tag{13}$$

where $\Gamma = {f_{rs}}^2 + \lambda_{ms} f_{rs} f_{ms} + {f_{ms}}^2$, and $\lambda_{ms} = Z_{ms}\,/\,Z_{rs}$ respectively. The frequency-domain characteristics of the internal impedance Z_{o0} are drawn in Fig. 6 with a set of numerical example as $L_1 = L_2 = 19\,\mu\mathrm{H}$, $C_1 = C_2 = 5.3\,\mathrm{nF}$, $R_o = 40\,\Omega$ and $f_r = 500\,\mathrm{kHz}$ while taking the variations of co-efficient k into consideration. In addition, the characteristics of driving-point impedance Z_{in} are depicted in Fig. 7 on the basis of (6) with the load resistance variation. The natural oscillation frequencies f_{n1} and f_{n2} are identical with ZPA frequencies where the phase angle $\angle \dot{Z}_{in}$ is zero.

The resonant frequency f_r deviates from the ZPA frequencies when the bifurcation occurs [35]. The resonant frequency is divided into two points for $k = 0.15$ and $k = 0.33$ in Fig. 6, and correspond to f_{n1} and f_{n2} in Figs. 7 (a) and (b). On the other hand, the resonant frequency f_r, which is marked by $\triangle$ in Fig. 6 corresponds to the natural oscillation frequency f_n marked by $\bigcirc$ in Fig. 7 (c) under the condition $k = 0.08$ and $R_o = 40\,\Omega$. Fig. 7 reveals $\angle \dot{Z}_{in}$ is almost linear to f_s as expressed by $\angle \dot{Z}_{in} = \alpha(k) f_s$ where $\alpha(k)$ is a proportional gain dependent on the coupling coefficient k.

The switching frequency deviation Δf_s from f_n or f_{n2} of ZPA are determined by giving the constant value θ_{ref} as the phase difference command as

$$\Delta f_s = \frac{\theta_{ref}}{\alpha(k)}. \tag{14}$$

It should be remarked herein the lower ZPA frequency f_{n1} is not suitable for tuning in the HF inverter since two frequencies exist for satisfying the reference angle θ_{ref}. The algorithm of RFT for the class-D HF inverter-based IPT system is presented by a flow chart in Fig. 8. The initial switching frequency is set in greater than f_r in order to avoid falling into the local ZPA frequency f_{n1}. The low-limit of switching frequency $f_{s,min}$ is set in f_r once the maximum gap length, i.e. the minimum coupling co-efficient is determined. The switching frequency f_s increases until the phase difference matches θ_{ref}. In the case of bifurcation, the greater ZPA frequency f_{n2} should be searched and f_s to be tuned to correspond with θ_{ref} so that Z_{in} is inductive and ZVS can be kept.

The turn-off current i_{Q1} is load-independent due to the near zero crossing current as long as the Tx-coil current i_p is formed by series resonance. Accordingly, the dead time t_d can be fixed with the limited range of switching frequency variation as $f_{s,min} \le f_s \le f_{s,max}$. In order to achieve ZVS turn-on of $\mathrm{Q_2}$ ($\mathrm{Q_1}$) while ensure the nearly ZCS turn-off of $\mathrm{Q_1}$ ($\mathrm{Q_2}$), the relevant time duration should be designed as

$$\frac{\theta_{ref}}{2\pi f_{s,max}} < t_d < \frac{\theta_{ref}}{2\pi f_{s,min}} \tag{15}$$

Thus, the dead time t_d can be naturally tuned in accordance with the switching frequency while the reference angle $\theta_{ref} = \angle \dot{Z}_{in}$ should be set so as to satisfy (15).

IV. Experiment Results and Discussions

The feasibility of the proposed IPT converter is investigated by experiment of a $400\,\mathrm{W}$-$500\,\mathrm{kHz}$ as a nominal frequency. The exterior appearance of the prototype is displayed in Fig. 9. The essential circuit parameters are listed in TABLE II. The inductive circular windings are adopted for the Tx and Rx coils respectively as sketched in Fig. 10, and their parameters are summarized in TABLE III. RFT-$\Delta\Sigma$PDM is implemented by the analog and digital logic circuits as depicted in Fig. 11. Bluethooth wireless module that has industry, science and medical (ISM) band of operating frequency (e.g. $2.4\,\mathrm{GHz}$) is applicable between the Tx and Rx coils. The command phase angle θ_{ref} is set as 13° in the RFT controller so that the power factor of the class-D HF inverter achieves by 0.97. The Tx and Rx coils are constructed of circular shape windings with Litz wires (44×7 twisted, $\phi = 0.12\,\mathrm{mm}$).

This article has been accepted for publication in a future issue of this journal, but has not been fully edited. Content may change prior to final publication. Citation information: DOI 10.1109/JESTIE.2021.3102445, IEEE Journal of Emerging and Selected Topics in Industrial Electronics

$$Z_{in} = \sqrt{\frac{{Z_{rs}}^2\left[\left\{1-\left(\frac{f_s}{f_{rs}}\right)-\lambda\left(\frac{f_s}{f_{rs}}\right)^2\right\}^2+{Q_{ms}}^2\left(\frac{f_s}{f_{ms}}\right)^2\left\{1+\left(\frac{f_{ms}}{f_{rs}}\right)^2+\lambda\left(\frac{f_{ms}}{f_{rs}}\right)^2-\left(\frac{f_s}{f_{rs}}\right)^2-\left(\frac{f_{ms}}{f_{rs}}\right)^2-\left(\frac{f_{ms}}{f_s}\right)\right\}\right]}{\left(\frac{f_s}{f_{rs}}\right)^2\left[1+\left\{Q_{ms}\left(\frac{f_{ms}}{f_s}-\frac{f_s}{f_{ms}}\right)\right\}^2\right]}} \tag{11}$$

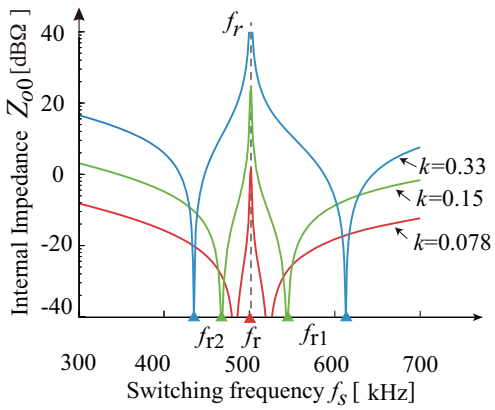

Fig. 6. Frequency-domain characteristics of the internal impedance Z_{o0}.

TABLE II
CIRCUIT PARAMETERS OF PROTOTYPE

Item	Symbol	Value [unit]
DC input voltage	V_{in}	100 V
Output power rating	P_o	400 W
Switching frequency range	f_s	501 kHz
Primary-side resonant capacitor	C_1	5.3 nF
Secondary-side resonant capacitor	C_2	5.3 nF
Output smoothing capacitor	C_o	10 μF
Dead time interval	t_d	150 ns
Electric load resistor	R_o	40 Ω

∗ SJ-MOSFET Q_1, Q_2: IPW50R190CE, 550 V, 18.5 A, 190 mΩ
∗ D_{o1}-D_{o4} : C3D20060D, 600 V, 28 A, 1.5 V@25°

TABLE III
SPECIFICATIONS OF TX AND RX COILS

Item	Symbol	Value [unit]
Windings turns	N_1/N_2	5 / 5
Self inductance of Tx coil	L_1	19 μH
Self inductance of Rx coil	L_2	19 μH
Mutual inductance of L_1 and L_2	M	1.52 μH (min.)
Quality factor of Tx and Rx coils	Q	98–108
Coupling coefficient of L_1 and L_2	k	0.08-0.15
Air gap length between L_1 and L_2	g	100 − 130 mm

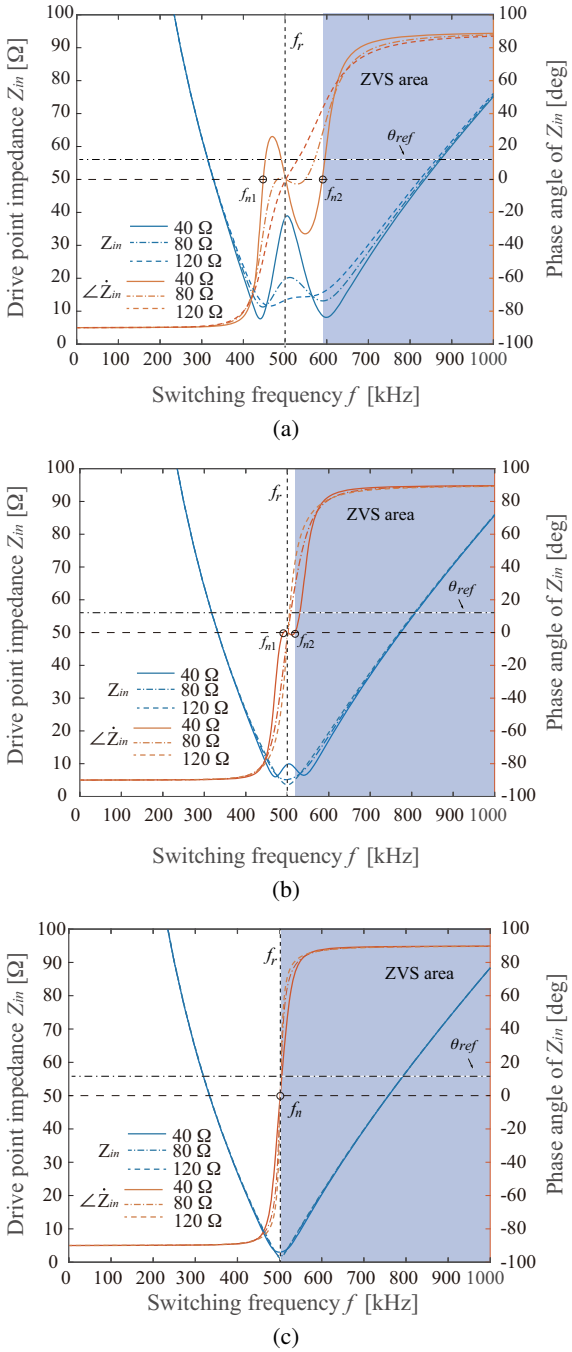

Fig. 7. Characteristics on the driving point impedance in the SS topology: (a) $k = 0.3$, (b) $k = 0.15$, and (c) $k = 0.08$ (numerical examples; $L_1 = L_2 = 19\,\mu$H, $C_1 = C_2 = 5.3$ nF, $R_o = 40\,\Omega$, 80 Ω, 120 Ω, and $f_r = 500$ kHz).

A. Essential Performances of RFT-PDM

The operating waveforms for the gap-length variations are depicted in Fig. 12 at the constant output voltage $V_o = 100$ V. In Fig. 12 (a) for $g = 110$ mm, the switching frequency f_s is controlled to 518 kHz while f_s is 511 kHz at $D_p = 0.85$ for $g = 130$ mm in Fig. 12 (b). As a result, ZVS operations can

This article has been accepted for publication in a future issue of this journal, but has not been fully edited. Content may change prior to final publication. Citation information: DOI 10.1109/JESTIE.2021.3102445, IEEE Journal of Emerging and Selected Topics in Industrial Electronics

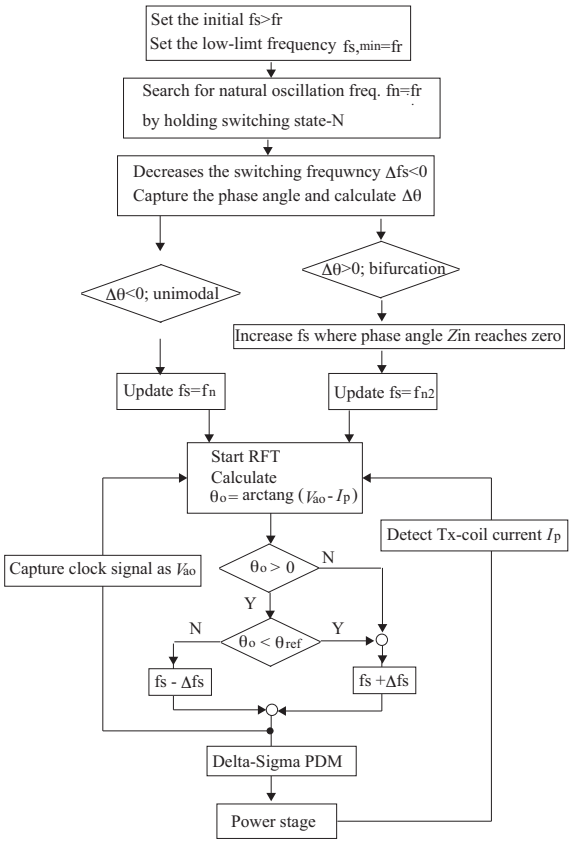

Fig. 8. Flow chart of RFT-ΔΣPDM algorithm.

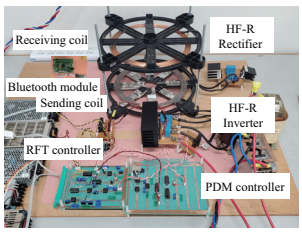

Fig. 9. Exterior appearance of IPT system.

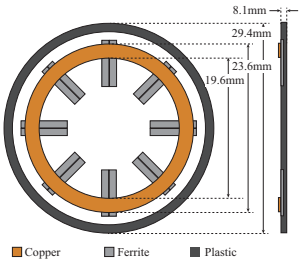

Fig. 10. Schematic view of Tx and Rx circular coils.

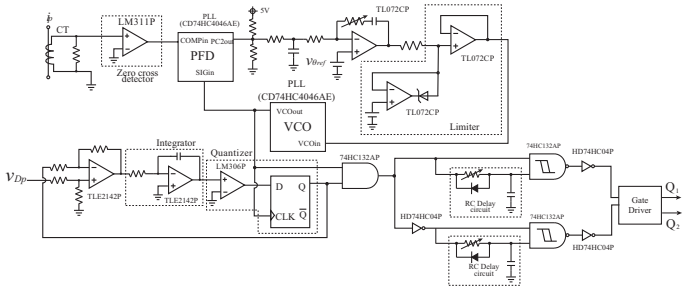

Fig. 11. Logic circuit diagram of RFT-ΔΣ PDM.

be observed in the switching voltages and currents of Q_1 and Q_2 in every cycle of power-ON and -OFF periods as well as their interchanging transitions in the PDM patterns.

The switching voltage and current waveforms are compared in Fig. 13 between CF-ΔΣPDM and RFT-ΔΣPDM. The power factor of the class-D HF inverter aggravates with the CF-ΔΣPDM, then the turn-off currents of Q_1 and Q_2 are relatively high as show in Fig. 13 (a). Accordingly, dv/dt rate increases at the turn-off transitions, then the hard switching emerges both in the high and low-side switches of the HF inverter. The actual efficiency of dc-dc power conversion is 71.5 % with $f_s = 530\,\mathrm{kHz}$ by CF-ΔΣPDM. In contrast, Fig. 13 (b) reveals the switching voltage and current waveforms with RFT-ΔΣPDM. The phase angle between the voltages and currents are well regulated in accordance with its command $\theta_{ref} = 13°$, thereby the turn-off currents of Q_1 and Q_2 are reduced so as to attain the nearly ZCS turn-off at $f_s = 511\,\mathrm{kHz}$. As a result, the actual efficiency improves up to 77.6 % due to the effect of RFT, which proves the validity of the proposed solution.

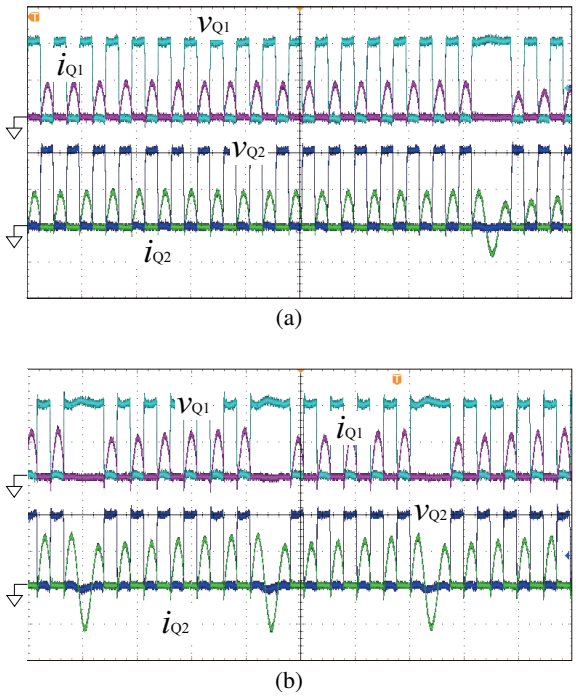

Fig. 12. Observed waveforms at the constant output voltage $V_o = 100\,\mathrm{V}$: (a) $g = 110\,\mathrm{mm}$ with $f_s = 518\,\mathrm{kHz}$ and $D_p = 0.98$, and (b) $g = 130\,\mathrm{mm}$ with $f_s = 511\,\mathrm{kHz}$ and $D_p = 0.85$(v_{Q1}, v_{Q2}: 50 V/div, i_{Q1}, i_{Q2}: 10 A/div, 4 μs/div).

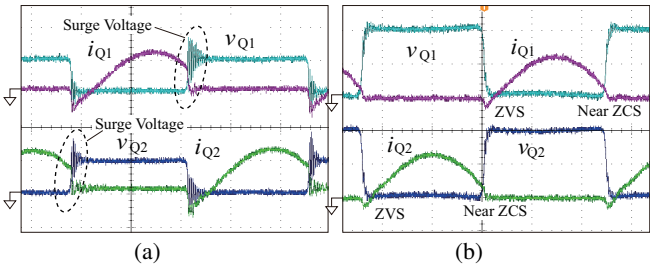

Fig. 13. Enlarged voltage and current waveforms at $g = 130\,\mathrm{mm}$ and $R_o = 40\,\Omega$:(a) CF-ΔΣPDM with $f_s = 530\,\mathrm{kHz}$ fixed (v_{Q1}, v_{Q2}: 100 V/div, i_{Q1}, i_{Q2}: 10 A/div, 400 ns/div), and (b) RFT-ΔΣPDM with $f_s = 511\,\mathrm{kHz}$ (v_{Q1}, v_{Q2}: 50 V/div, i_{Q1}, i_{Q2}: 10 A/div, 400 ns/div).

This article has been accepted for publication in a future issue of this journal, but has not been fully edited. Content may change prior to final publication. Citation information: DOI 10.1109/JESTIE.2021.3102445, IEEE Journal of Emerging and Selected Topics in Industrial Electronics

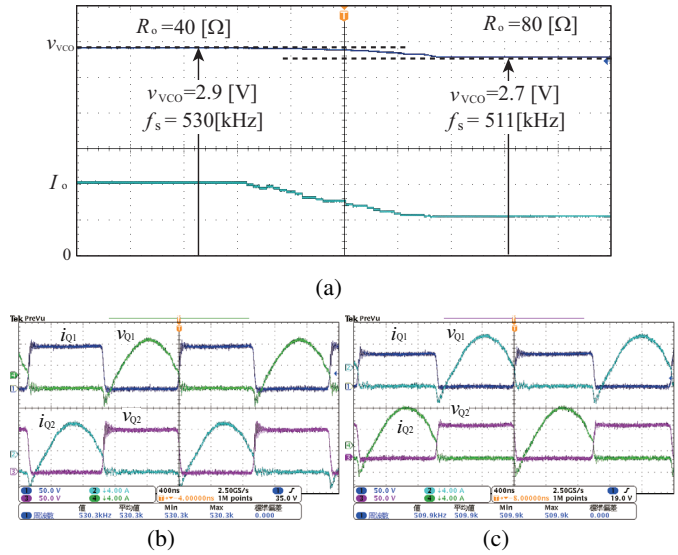

Fig. 14. Transitional waveforms for the load variation at $V_o = 100\,\mathrm{V}$ and $g = 100\,\mathrm{mm}$: (a) VCO input signal and dc load current (v_{vco}:0.5 V/div, I_o:10 A/div, 100 ms/div), (b) switching waveforms for $R_o = 40\,\Omega$, and (c) switching waveforms for $R_o = 80\,\Omega$ (v_{Q1}, v_{Q2}:50 V/div, i_{Q1}, i_{Q2}:4 A/div, 400 μs/div).

B. Performances for Load Variations and Gap length

The dynamical performance on the load variation is revealed in Fig. 14, where the input signal V_{vco} of the voltage controlled oscillator (VCO) in the controller and the load dc current I_o are exhibited. It should be remarked that the coil gap-length is set as $g = 100\,\mathrm{mm}$ and $k = 0.3$ for assuming the bifurcation condition. The switching frequency f_s is tracked successfully in accordance with the variation of load resistance R_o; from $f_s = 530\,\mathrm{kHz}$ with $R_o = 40\,\Omega$ and $D_p = 1$ to $f_s = 511\,\mathrm{kHz}$ with $R_o = 80\,\Omega$ and $D_p = 0.63$ in the controller stage. Fig.14 reveals the switching performances before and after the load variation. The ZVS turn-on and nearly ZCS turn-off operations attain with the switching frequency adjustment from $f_s = 530.3\,\mathrm{kHz}$ to $f_s = 509.9\,\mathrm{kHz}$ in the power stage. Thus, it is verified that the proposed control method can accommodate the load variation under the condition of bifurcation by adjusting the switching frequency and the pulse density simultaneously in the Tx-side power stage.

The steady-state characteristics of the output power versus pulse density are depicted in Fig. 15. It can be confirmed that output power is controlled as the quadratic function of D_p over the wide range; 4 W–400 W (1 % –100 % load) by Δ-Σ PDM, thereby the validity of (5) is clearly revealed herein.

The output voltages for the gap length variations are depicted in Fig. 16 under the conditions of RFT with or without Δ-Σ PDM. The latter pulse modulation is similar to PFM by which only the load resonance is considered and the driving point impedance is tuned in order to keep ZPA. The output voltage can be regulated at $V_o = 100\,\mathrm{V}$ constant by adopting RFT. Thus, effectiveness of the Δ-Σ PDM incorporating into the resonant frequency tuning is effective for output power control in the IPT applications. The actual efficiencies are compared with the fixed load between CF- and RFT-$\Delta\Sigma$PDMs for the various gap-length conditions; from the unimodal to

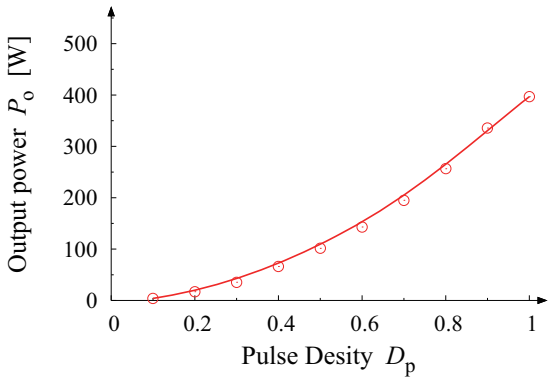

Fig. 15. Measured characteristics of the output power versus pulse density by RFT-$\Delta\Sigma$ PDM at $g = 150\,\mathrm{mm}$.

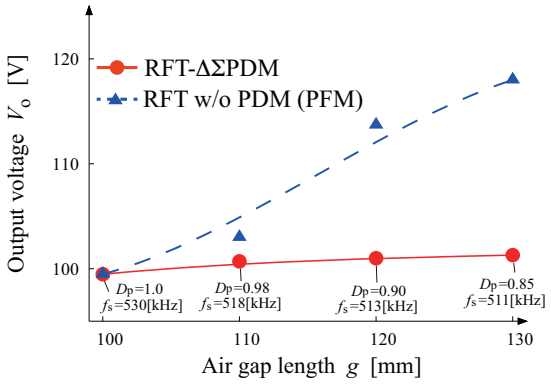

Fig. 16. Measured curves of the output voltage and air gap length at $V_o = 100\,\mathrm{V}$ and $R_o = 40\,\Omega$.

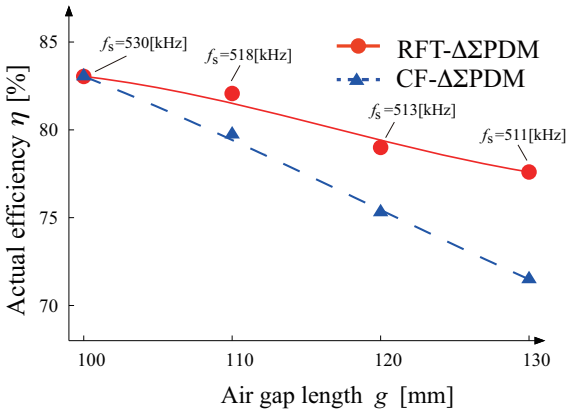

Fig. 17. Measured curves of actual efficiency versus air gap length for $R_o = 40\,\Omega$ under the conditions $(D_p, g) = (1.0, 100), (0.98, 110), (0.9, 120), (0.8, 130)$.

spurious profiles. Note here the switching frequency is set at 530 kHz in CF-$\Delta\Sigma$PDM in order to accommodate for the same range of g as RFT-$\Delta\Sigma$PDM. It can be observed the higher efficiency can attain by adopting RFT-$\Delta\Sigma$PDM.

The output power characteristics with RFT-$\Delta\Sigma$PDM at the minimum and maximum gap lengths are presented in Fig. 18, whereby the load impedance variations of battery chargers are assumed. The output power can widely be regulated at the

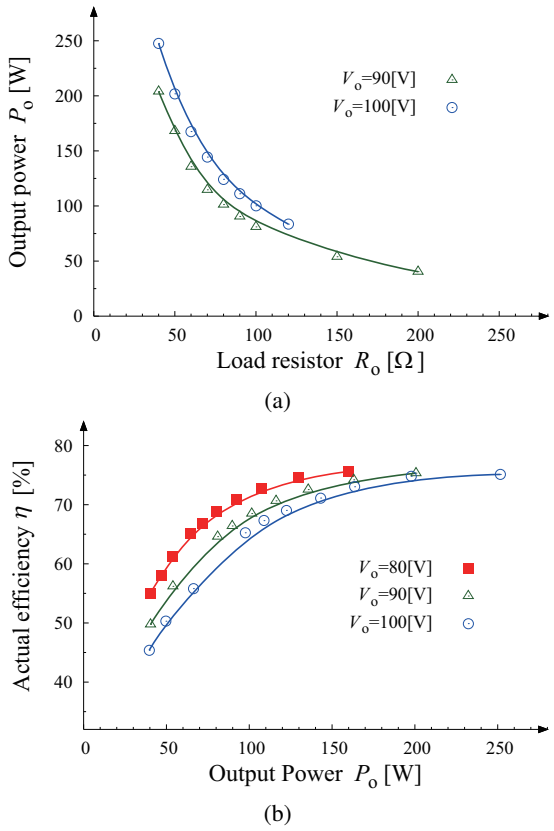

Fig. 18. Measured characteristics for the load variations with the output voltage closed loop: (a) $g = 100\,\mathrm{mm}$, and (b) $g = 130\,\mathrm{mm}$.

constant voltage by tuning both of D_p and f_s in the proposed controller and calculation algorithm. Thus, feasibility of the RFT-ΔΣPDM controlled IPT is verified in the case of battery charger applications.

The steady-state curves for the load variations are depicted in Fig 18. The actual efficiency of dc-dc power conversion maintains over $80\,\%$ from the middle to heavy load conditions as displayed in Fig 18.

C. Efficiency and Power Loss Analysis

The actual efficiency versus the air gap length are compared between CF- and RFT-ΔΣPDMs and under the same conditions of PDM factor and load resistance in Fig.17. The maximum efficiency is recorded as $83.4,\%$ at $g = 100\,\mathrm{mm}$, $D_p = 1$ and $f_s = 530\,\mathrm{kHz}$. The power loss analysis is displayed in Fig. 19. The ratio of switching power loss which appears at the turn-off transitions accounts for $14.5\,\%$ in CF-ΔΣPDM due to the hard switching turn-off. However, it is alleviated with the aid of RFT-ΔΣPDM, then the switching power loss reduces to $4.9\,\%$; the efficiency increases by $6.1\,\%$, compared to CF-ΔΣPDM.

The copper losses of Tx and Rx coils account for about $20\,\%$ respectively in RFT-ΔΣPDM. The conduction losses of the switches and diodes account for about $40\,\%$ in total. This is due to the de-rating of the input dc voltage as compared to the switch and diode voltage rating for avoiding the saturation of Tx and Rx coils magnetic ferrite cores. Hence, the efficiency

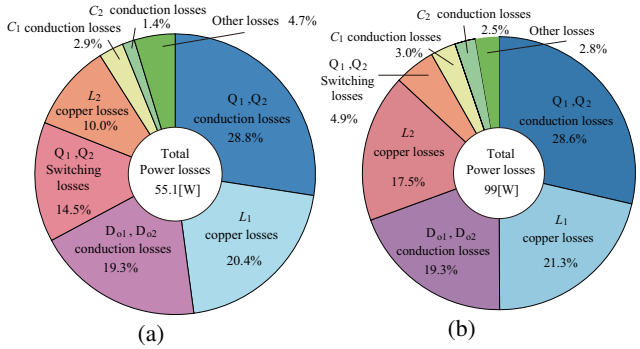

Fig. 19. Power loss analysis at $g = 130\,\mathrm{mm}$ and $R_o = 40\,\Omega$: (a) CF-ΔΣ PDM for $P_o = 142\,\mathrm{W}$ and $\eta = 70.2\,\%$ and (b) RFT-ΔΣ PDM for $P_o = 346\,\mathrm{W}$ and $\eta = 77\,\%$.

can be expected to improve by optimizing the coils design with less leakage magnetic fluxes as well as the adoption of wide bang gap power devices.

V. Conclusion

The resonant frequency tuning Δ-Σ transformation PDM controlled class-D resonant converter for inductive wireless power transfer has been proposed in this paper. The transmitted power from the primary-side class-D HF inverter is compensated and maximized with the switching frequency based on the resonant frequency tuning. The power factor of the class-D HF inverter is improved by the effect of the resonant frequency tuning, thereby zero voltage soft switching can achieve over the wide range of output power. The transmitter and receiver coil currents are regulated by RFT-ΔΣPDM without any significant subharmonics through the whole range of pulse density factor.

The feasibility of the proposed IPT system has been verified by experiment of a $400\,\mathrm{W}$ prototype; the maximum efficiency achieves $83.4\,\%$ at $g = 100\,\mathrm{mm}$, and the flat curve of efficiency can maintain around $75\,\%$ from the full to $5\,\%$ load under the condition of ZVS at the gap length $g = 150\,\mathrm{mm}$. The output power can be controlled from $1\,\%$ to $100\,\%$ loads can achieve by RFT-ΔΣ PDM as well as the constant output voltage regulation for the gap length variations $g = 110\,\mathrm{mm}$–$130\,\mathrm{mm}$. The efficiency improves by $6.1\,\%$ at $g = 130\,\mathrm{mm}$ due to the effect of resonant frequency tuning in comparison with the constant frequency ΔΣ PDM.

References

[1] M. Fu, H. Yin, X. Zhu, and C. Ma, "Analysis and tracking of optimum load in wireless power transfer systems," *IEEE Trans. Power Electron.*, vol.30, no.7, pp.3952-3963, Jul. 2015.

[2] P.M. Fan and M. Daut, "Near-unity power factor, voltage step-up/down conversion pulse-width modulated switching rectification for wireless power transfer receiver," *IEEE Trans. Power Electron.*, vol.34, no.11, pp.10960-10969, Nov. 2019.

[3] M. Kim, D.M. Joo, B.K. Lee, "Design and control of inductive power transfer system for electric vehicles considering wide variation of output voltage and coupling coefficient," *IEEE Trans. Power Electron.*, vol.34, no.2, Feb. 2019.

[4] K. Colak, E. Asa, M. Bojarski, D. Czarkowski and O. C. Onar, "A novel phase-shift control of semibridgeless active rectifier for wireless power Transfer," *IEEE Trans. Power Electron.*, vol.30, no.11, pp.6288-6297, Nov. 2015.

[5] E. Ozalevli, N. Femia, G. Di Capua, R. Subramonian, D. Du, J. Sankman, and M. El Markhi, "A cost-effective adaptive rectifier for low power loosely coupled wireless power transfer systems," *IEEE.Trans. Circuits Syst. 1: Reg. Papers*, vol.65, no.7, pp.2318-2319, Jul. 2018.

[6] Y. Fang and B. Pong, "Multiple Harmonics Analysis for Variable Frequency Asymmetrical pulsewidth-modulated wireless power transfer systems," *IEEE Trans. Ind. Electron.*, vol.66, no.5, pp.4023-4030, May 2019.

[7] D. Thrimawithana and U.K. Madawala, "A generalized steady-state model for bidirectional IPT systems," *IEEE Trans. Power Electron.*, vol.28, no.10, pp.4681-4689, Oct. 2013.

[8] T. Diekhans and R.W. De Doncker, "A dual-side controlled inductive power transfer system optimized for large coupling factor variations and partial load," *IEEE Trans. Power Electron.*, vol.30, no.11, Nov. 2015.

[9] V-B. Vu, D-H. Tran, and W. Choi, "Implementation of the constant current and constant voltage charge of inductive power transfer systems with the double-sided LCC compensation topology for electric vehicle battery charger applications," *IEEE Trans. Power Electron.*, vol.33, no.9, pp.7398-7410, Sep. 2018.

[10] E. Gati, G. Kampitsis, and S. Manias, "Variable frequency controller for inductive power transfer in dynamic conditions," *IEEE Trans. Power Electron.*, vol.32, no.2, pp.1684-1696, Feb. 2017.

[11] Z. Yan, Y. Zhang, T. Kan, F. Lu, K. Zhang, B. Song, and C.C. Mi, "Frequency optimization of a loosely coupled underwater wireless power transfer system considering eddy current loss, *IEEE Trans. Ind. Electron.*, vol.66, no.5, pp.3468-3476, May 2019.

[12] Y. Zhang, T. Kan, Z. Yan. and C. Mi, "Frequency and voltage tuning of series-series compensated wireless power transfer system to sustain rated power under various conditions," *IEEE Trans. Power Electron.*, vol.7, no.2, pp.1311-1317, Jun. 2019.

[13] H.Y. Leung, D. Mccormick, D.M. Budgett, and A.P. Hu, "Pulse density modulated control patterns for inductively powered implantable devices based on energy injection control," *IET Power Electron.*, vol.6, no.6, pp.1051-1057, Jul. 2013.

[14] H. Li, J. Fang, S. Chen, K. Wang, and Y. Tang, "Pulse density modulation for maximum efficiency point tracking of wireless power transfer systems," *IEEE Trans. Power Electron.*, vol.33, no.6, pp.5492-5501, Jun. 2019.

[15] M. Fan, L. Shi, Z. Yin, L. Jiang, and F. Zhang, "Improved pulse density modulation for semi-bridgeless active rectifier in inductive power transfer system," *IEEE Trans. Power Electron.*, vol.34, no.6, pp.5893-5902, Jun. 2019.

[16] T. Mishima and E. Morita, "High-frequency bridgeless rectifier based ZVS multiresonant converter for inductive power transfer featuring high-voltage GaN HFET," *IEEE Trans. Ind. Electron.*, vol.64, no.11, pp.9155-9164, Nov. 2017.

[17] T. Mishima and M. Nakaoka, "A load power adaptive dual pulse modulated current phasor-controlled ZVS high-frequency resonant inverter for induction heating applications," *IEEE Trans. Power Electron.*, vol.29, no.8, pp.3864-3880, Aug. 2014.

[18] S. Chen, H. Li, and Y. Tang, "Extending the operating region of inductive power transfer systems through dual-side cooperative control," *IEEE Trans. Ind. Electron.*, vol.67, no.11, pp.9302-9312, Nov. 2020.

[19] X. Sheng and L. Shi, "An improved pulse modulation strategy based on harmonics on ICPT system," *IEEE Trans. Power Electron.*, vol. 35, no. 7, pp. 6810-6819, July 2020.

[20] D. Wu, R. Mai, S. Zhao, Z. He, and F. Peng, "A self-oscillating controller based on pulse density modulator in wireless power transfer," *Proc. 2019 IEEE Energy Conv. Congr. Exp.* (ECCE), pp.2125-2128, Sep. 2019.

[21] A. Berger, M. Agostinelli, S. Võesti, J.A.Oliver, J.A. Cobos and M.Huemer, "A wireless charging system applying phase-shift and amplitude control to maximize efficiency and extractable power," *IEEE Trans. Power Electron.*, vol.30, no.11, pp. 6338-6348, Nov. 2015.

[22] S. Hong *et al.*, "A frequency-selective EMI reduction method for tightly coupled wireless power transfer systems using resonant frequency control of a shielding coil in smartphone application," *IEEE Trans. Electromag. Compt.*, vol.61, no.6, pp.2031-2039, Dec. 2019.

[23] M. Ibrahim, L. Bernard, L. Pichon, E. Laboure, A. Razek, O. Cayol, D. Ladas, and J. Irving, "Inductive charger for electric vehicle: advanced modeling and interoperability analysis," *IEEE Trans. Power Electron.*, vol.31, no.12, pp.8096-8114, Dec. 2016.

[24] P.M. Aziz, H.V. Sorensen, and J. Spiegel, "An overview of sigma-delta converters," *IEEE Signal Process. magz.*, vol.8, no.1, pp.61-84, Jan. 1991.

[25] M. Ibrahim, L. Bernard, L. Pichon, E. Laboure, A. Razek, O. Cayol, D. Ladas, and J. Irving, "Inductive charger for electric vehicle: advanced modeling and interoperability analysis," *IEEE Trans. Power Electron.*, vol.31, no.12, pp.8096-8114, Dec. 2016.

[26] M. Moghaddami, A. Sundararajan, and A.I. Sarwat, "A power-frequency controller with resonance frequency tracking capability for inductive power transfer systems," *IEEE Trans. Ind. Appl.*, vol.54, no.2, pp.1773-1783, Mar./Apr., 2018.

[27] S. Valtchev, B. Borges, K. Brandisky, and J.B. Klaassens, "Resonant contactless energy transfer with improved efficiency," *IEEE Trans. Power Electron.*, vol.24, no.3, pp.685-699, Mar. 2009.

[28] X. Qu, Y. Yao, D. Wangf, S.-C. Wong, and C.K. Tse, "A family oh hybrid IPT topologies with near load-independent output and high tolerance to pad misalignment," *IEEE Trans. Power Electron.*, vol.35, no.7, pp.6867-6876, Jul., 2020.

[29] K. Agarwal, R. Jegadeesan, Y.X. Guo, and N.V. Takor, —*IEEE Rev. Biomed. Eng.*, vol.10, pp.136-161, 2017.

[30] S. Samanta and A.K. Rathore, "Analysis and design of load-independent ZPA operation for P/S, PS/S, P/SP, and PS/SP tank networks in IPT applications," *IEEE Trans. Power Electron.*, vol.33, no.8, pp.6476-6482, Aug. 2018.

[31] R.D. Middlebrook, V. Vorpérian, and J. Lindal, "The *N* extra element theorem," *IEEE Trans. Circuits and Systems –I: fundamental theory and applications*, vol.45, no.9, pp.919-935, Sep. 1998.

[32] H. Li, S. Chen, J. Fang, Y. Tang, and M. de Rooij, "A low-subharmonics, full-range, and rapid pulse density modulation strategy for ZVS full-bridge converters," *IEEE Trans. Power Electron.*, vol.34, no.9, pp.8871-8881, Sep. 2019.

[33] Y. Li, X. Ruan, L. Zhang, and J. Dai, "Optimized parameters design for a 20 MHz class E dc-dc converter with on-off control," *Proc. 2018 IEEE Energy Conv. Congr. and Expo.* (ECCE), pp.2164-2170, Sep. 2019.

[34] Y.H. Sohn, B.H. Choi, E.S. Lee, G.C. Lim, G.H Cho, and C.T. Rim, "General unified analyses of two-capacitor inductive power transfer systems: equivalence of current-source SS and SP compensations," *IEEE Trans. Power Electron.*, vol.30, no.11, pp.6030-6045, Nov. 2015.

[35] N-C. Kuo, B. Zhao, and A.M. Niknejad, "Bifurcation analysis in weakly-coupled inductive power transfer systems," *IEEE.Trans. Circuits Syst. 1: Reg. Papers*, vol.63, no.5, pp.727-738, May 2016.

Tomokazu Mishima (S'00–M'04–SM'15) received the Ph.D. degree in electrical engineering from The University of Tokushima, Japan in 2004. Since 2010, he has been with Kobe University, Hyogo, Japan as an associate professor, and engages in the researches and developments of power electronics circuits and systems. Dr. Mishima has been appointed to the Center for Advanced Medical Engineering Research and Development (CAMED), Kobe University since 2020, where he engages in research and development of wireless power transfer systems for implantable devices. His research interests include soft-switching dc–dc converters, resonant converters, and high frequency inverters for industrial, automotive, biomedical, renewable and sustainable energy applications. He is the recipients of several paper awards in the IEEE-sponsored conferences. He is a senior member of IEEJ (The Institute of Electrical Engineering of Japan), and a member of IEICE (The Institute of Electronics, Information and Communication Engineers).

Ching-Ming Lai (S'06–M'10–SM'17) received the Ph.D. degree in electrical engineering from National Tsing Hua University (NTHU), Hsinchu, Taiwan, in 2010. Since 2019, Dr. Lai is an Associate Professor with the Department of Electrical Engineering in National Chung Hsing University (NCHU), Taiwan, where he is also the director of intelligent electric vehicle green energy center (i-Center). He is the recipients of several paper awards in the IEEE-sponsored conferences. Dr. Lai is a Fellow of the Institution of Engineering and Technology (IET), a Fellow of the Australian Institute of Energy (AIE), and a Life Member of the Taiwan Power Electronics Association (TaiPEA).